

PAPER • OPEN ACCESS

## Bayesian modelling of multiple plasma diagnostics at Wendelstein 7-X





To cite this article: Sehyun Kwak *et al* 2024 *Nucl. Fusion* **64** 106022

View the [article online](#) for updates and enhancements.

You may also like

- [Turbulence-reduced high-performance scenarios in Wendelstein 7-X](#)  
O.P. Ford, M. Beurskens, S.A. Bozhenkov et al.
- [Broadband Alfvénic excitation correlated to turbulence level in the Wendelstein 7-X stellarator plasmas](#)  
S. Vaz Mendes, K. Rahbarnia, C. Slaby et al.
- [The Set of Diagnostics for the First Operation Campaign of the Wendelstein 7-X Stellarator](#)  
Ralf König, J. Baldzuhn, W. Biel et al.

# Bayesian modelling of multiple plasma diagnostics at Wendelstein 7-X

Sehyun Kwak<sup>1,\*</sup> , U. Hoefel<sup>2</sup> , M. Krychowiak<sup>1</sup>, A. Langenberg<sup>1</sup> , J. Svensson<sup>2</sup>, H. Trimino Mora<sup>1</sup>, Y.-C. Ghim<sup>3</sup>  and the W7-X Team<sup>a</sup>

<sup>1</sup> Max-Planck-Institut für Plasmaphysik, 17491 Greifswald, Germany

<sup>2</sup> Seed eScience Research Ltd, London W1W 8DH, United Kingdom of Great Britain and Northern Ireland

<sup>3</sup> Department of Nuclear and Quantum Engineering, KAIST, Daejeon 34141, Korea, Republic Of

E-mail: [sehyun.kwak@ipp.mpg.de](mailto:sehyun.kwak@ipp.mpg.de)

Received 12 April 2024, revised 28 June 2024

Accepted for publication 12 August 2024

Published 27 August 2024



CrossMark

## Abstract

Inference of electron density and temperature has been performed using multiple, diverse sets of plasma diagnostic data at Wendelstein 7-X. Predictive models for the interferometer, Thomson scattering and helium beam emission spectroscopy (He-BES) systems have been developed within the Minerva framework and integrated into a unified model. Electron density and temperature profiles are modelled using Gaussian processes. Calibration factors for the Thomson scattering system and predictive uncertainties are considered as additional unknown parameters. The joint posterior probability distribution for the electron density and temperature profiles as well as Gaussian process hyperparameters and model parameters is explored through a Markov chain Monte Carlo algorithm. Samples from this distribution are numerically marginalised over the hyperparameters and model parameters to yield marginal posterior distributions for the electron density and temperature profiles. The profile inferences incorporate various data combinations from the interferometer and Thomson scattering as well as constraints at the limiter/divertor positions through *virtual observations* or edge data from He-BES. Additionally, the integration of x-ray imaging crystal spectrometer data into the model for ion temperature profiles is presented. All profiles presented in this study are inferred with optimally selected hyperparameters and model parameters by exploring the joint posterior distribution, inherently applying Bayesian Occam's razor.

Keywords: Bayesian inference, plasma diagnostics, synthetic diagnostics, Gaussian processes, Wendelstein 7-X

(Some figures may appear in colour only in the online journal)

<sup>a</sup> See Grulke *et al* 2024 (<https://doi.org/10.1088/1741-4326/ad2f4d>) for the W7-X Team.

\* Author to whom any correspondence should be addressed.



Original Content from this work may be used under the terms of the [Creative Commons Attribution 4.0 licence](https://creativecommons.org/licenses/by/4.0/). Any further distribution of this work must maintain attribution to the author(s) and the title of the work, journal citation and DOI.

## 1. Introduction

Consistent inference of fusion plasma physics parameters and their associated uncertainties is essential for understanding and controlling the physical phenomena in large-scale fusion experiments. Experiments such as Joint European Torus (JET) [1] or Wendelstein 7-X (W7-X) [2] typically utilise dozens of sophisticated measurement techniques. Analysing experimental data from each measurement instrument is inherently complex, making the comprehensive utilisation of these diverse data sets to refine physics parameters a considerable challenge. To address this, employing a framework capable of managing parameters, assumptions, predictive models and observations is advantageous.

The Minerva framework has been developed to deliver consistent inference for complex systems through the modularisation of (predictive) forward models and standardisation of interfaces for systematic integration [3]. For instance, a Minerva model for Thomson scattering encapsulates physics and instrumental effects to compute Thomson scattering signals based on variables such as laser power and wavelength, scattering angles, spectral response functions and data acquisition systems alongside physics parameters like electron density and temperature. These model dependencies can be sourced from other Minerva models or external data sources, allowing for a direct comparison between model predictions and actual observations. Minerva automates the integration of these models, which can be depicted through a Bayesian graphical model [4], offering a transparent approach to managing model complexity. This automated model management and graphical representation enable the practical joint analysis of multiple heterogeneous data sets. In nuclear fusion research, the Minerva framework has been applied across a range of diagnostics, including magnetic sensors [5], interferometers [6, 7], Thomson scattering systems [8, 9], soft x-ray spectroscopy [10, 11], beam emission spectroscopy [12, 13], x-ray imaging crystal spectrometers (XICSs) [14, 15], electron cyclotron emission (ECE) [16] and effective ion charge diagnostics [17, 18]. Additionally, Minerva models can be accelerated using field-programmable gate arrays [19] or artificial neural networks [20–22].

In this study, we have conducted a Bayesian joint analysis of the dispersion interferometer (DI) [23], Thomson scattering (TS) [8] and helium beam emission spectroscopy (He-BES) systems [24] at W7-X, further enhanced by integrating the XICSs [15]. Traditionally, analyses of the DI, TS and He-BES systems have been conducted separately. The calibration factor of the TS system, when not fully determined, allows for electron density profiles from TS data to be cross-calibrated using DI data. Achieving precise cross-calibration requires knowledge of electron density and temperature in the plasma edge region, a challenge compounded by the predominance of electronics noise over TS signals in this area. This challenge is traditionally addressed by assuming electron density and temperature to be zero outside the last closed flux surface (LCFS). Our approach improves upon this by utilising

empirical constraints on electron density and temperature at limiter/divertor positions, introduced as *virtual observations* based on prior physics knowledge, or by employing measurements from the He-BES system. Furthermore, the integration of XICS into our Bayesian joint model enables a more comprehensive inference of electron density and temperature profiles, as well as ion temperature profiles, ensuring consistency across all diagnostic measurements.

We introduce several contributions to the field of fusion plasma diagnostics through our comprehensive Bayesian modelling approach. The integration of multiple plasma diagnostic systems at W7-X, including DI, TS and He-BES, within the Minerva framework, represents an advancement in achieving a unified analysis of plasma diagnostics. By employing advanced Bayesian modelling techniques, we not only facilitate the automatic cross-calibration of the TS system with DI data but also rigorously quantify predictive uncertainties, thereby enhancing the reliability of inferred plasma parameters. The incorporation of virtual observations, informed by prior physics knowledge, for effective cross-calibration and improved data analysis in regions with limited direct measurements, illustrates an application of empirical knowledge within a Bayesian framework.

## 2. The model

In Bayesian inference [4, 25, 26], the probability of a hypothetical value of unknown parameters, denoted as  $P(H)$ , can be updated to the posterior probability of the unknown parameters given observations, denoted as  $P(H|D)$ , through Bayes' theorem:

$$P(H|D) = \frac{P(D|H)P(H)}{P(D)}. \quad (1)$$

Here, the probability of the unknown parameters, also known as the prior probability  $P(H)$ , encodes *prior knowledge* including physical and empirical assumptions. For instance, since temperature must be positive by definition, the probability of any negative temperature value should be set to zero. The conditional probability of the observations given the unknown parameters,  $P(D|H)$ , represents a *predictive* distribution over the observations for a hypothetical value of the unknown parameters. This predictive distribution reflects all possible observation values that could be measured, given a hypothetical set of parameter values. Typically, the mean of the predictive distribution can be determined by a function that encapsulates the processes occurring during an experiment, taking into account physical phenomena as well as experimental setup factors such as instrument effects, calibration, optics and electronics. This function is known as a forward model and is represented by  $f(H)$ . The marginal probability of the observations  $P(D)$ , also referred to as the model evidence, is a normalization constant in this context.

When we have multiple heterogeneous data sets, which conditionally depend on the unknown parameters, Bayes' theorem can be written as:

$$P(H|\{D_i\}) = \frac{(\prod_i P(D_i|H)) P(H)}{P(\{D_i\})}. \quad (2)$$

Each predictive distribution includes a forward model of the measurement instruments, which are typically complex and sophisticated. These models may incorporate additional model parameters, such as calibration factors, depending on the experimental setup. The prior distribution encapsulates the prior knowledge of both the unknown parameters and the hyperparameters (parameters of the prior distribution) as well as unknown model parameters. Together, these prior and predictive distributions form the joint probability distribution  $P(H, D)$ , capturing the full relationship between all unknown parameters and observations. This joint distribution is represented in Minerva as a Bayesian graphical model [4].

The Minerva graph for the Bayesian joint model of the DI, TS and He-BES systems is depicted in figure 1. Each node in the graph represents either a deterministic calculation (white box) or a probability function, be it a prior (blue circle) or a predictive probability (grey circle). Deterministic nodes might perform simple operations (e.g. `los`, a function for line integration along a line of sight), represent a physics model (e.g. Thomson model) or signify a data source (`ds`). The arrows in the graph indicate the conditional dependencies among these nodes, illustrating the joint distribution of all unknown parameters and observations, comprised of all prior and predictive distributions.

In this work, the electron density  $n_e$  and temperature  $T_e$  profiles are modelled as functions of the effective minor radius  $\rho_{\text{eff}}$  using Gaussian processes [27–29]. Gaussian processes are *non-parametric* functions that associate any set of points within their domain with a random vector following a multivariate Gaussian distribution. Unlike parametric functions, the characteristics of Gaussian processes are determined by their covariance function. This function specifies the covariance (or correlation) between the function outputs for any two input points, affecting the smoothness of the Gaussian processes. In nuclear fusion research, Gaussian processes were first introduced for non-parametric tomography to map electron density and current distribution [7], and have since been utilised in a wide range of applications [9, 10, 12, 13, 15, 18, 30, 31].

In the model, the Gaussian process for the electron temperature is specified by a zero mean and a squared exponential covariance function, commonly used in Gaussian processes, and can be described as:

$$P(T_e|\sigma_{T_e}) = \mathcal{N}(0, \Sigma_{T_e}), \quad (3)$$

$$\Sigma_{T_e}(\rho_{\text{eff},i}, \rho_{\text{eff},j}) = \sigma_{f,T_e}^2 \exp\left(-\frac{(\rho_{\text{eff},i} - \rho_{\text{eff},j})^2}{2\sigma_{x,T_e}^2}\right) + \sigma_{y,T_e}^2 \delta_{ij}. \quad (4)$$

Here, the hyperparameters are denoted as  $\sigma_{T_e} = [\sigma_{f,T_e}, \sigma_{x,T_e}]$ .  $\sigma_f$  represents the overall scale, influencing the overall variance of the Gaussian process.  $\sigma_x$  is the characteristic length scale, determining the smoothness of the Gaussian process. The noise scale, denoted by  $\sigma_y$ , is set to a relatively small value compared to  $\sigma_f$ , for example,  $\sigma_y/\sigma_f = 10^{-3}$ , to mitigate numerical instabilities.

Given the potentially different smoothness (gradient) in the core and edge regions, the electron density prior distribution employs a Gaussian process with a zero mean and a non-stationary covariance function [32], represented as:

$$P(n_e|\sigma_{n_e}) = \mathcal{N}(0, \Sigma_{n_e}), \quad (5)$$

$$\Sigma_{n_e}(\rho_{\text{eff},i}, \rho_{\text{eff},j}) = \sigma_{f,n_e}^2 \left( \frac{2\sigma_{x,n_e}(\rho_{\text{eff},i})\sigma_{x,n_e}(\rho_{\text{eff},j})}{\sigma_{x,n_e}(\rho_{\text{eff},i})^2 + \sigma_{x,n_e}(\rho_{\text{eff},j})^2} \right)^{\frac{1}{2}} \times \exp\left(-\frac{(\rho_{\text{eff},i} - \rho_{\text{eff},j})^2}{\sigma_{x,n_e}(\rho_{\text{eff},i})^2 + \sigma_{x,n_e}(\rho_{\text{eff},j})^2}\right) + \sigma_{y,n_e}^2 \delta_{ij}. \quad (6)$$

The length scale function,  $\sigma_{x,n_e}(\rho_{\text{eff}})$ , is modelled using a hyperbolic tangent function as developed in [30]:

$$\sigma_{x,n_e}(\rho_{\text{eff}}) = \frac{\sigma_{x,n_e}^{\text{core}} + \sigma_{x,n_e}^{\text{edge}}}{2} - \frac{\sigma_{x,n_e}^{\text{core}} - \sigma_{x,n_e}^{\text{edge}}}{2} \times \tanh\left(\frac{\rho_{\text{eff}} - \rho_{\text{eff},0,n_e}}{\rho_{\text{eff},w,n_e}}\right). \quad (7)$$

The set of hyperparameters is denoted as  $\sigma_{n_e} = [\sigma_{f,n_e}, \sigma_{x,n_e}^{\text{core}}, \sigma_{x,n_e}^{\text{edge}}, \rho_{\text{eff},0,n_e}, \rho_{\text{eff},w,n_e}]$ .

The electron density and temperature profiles are mapped to  $x, y, z$  Cartesian coordinates using the coordinate transformations provided by the variational moments equilibrium code node [33, 34]. With the 3D fields of electron density and temperature in real space, predictive distributions for the data from the DI, TS and He-BES systems can be calculated. The single-chord DI system [23] measures the line-integrated electron density along the line of sight. Its forward model predicts this line integral of electron density, which is then directly compared to the measurements stored in the W7-X database. The TS system [8] captures Thomson scattered spectra from 10 to 79 spatial locations along the laser beam across the plasma centre. A physics model for the TS process [35] is incorporated into the Thomson model [8, 9], which predicts the Thomson scattered spectra based on the electron density and temperature. To account for uncertainties in the calibration factor of the TS system, the calibration factor is treated as an additional unknown parameter.

The joint posterior distribution for the Bayesian joint model of the DI and TS systems can be expressed as:

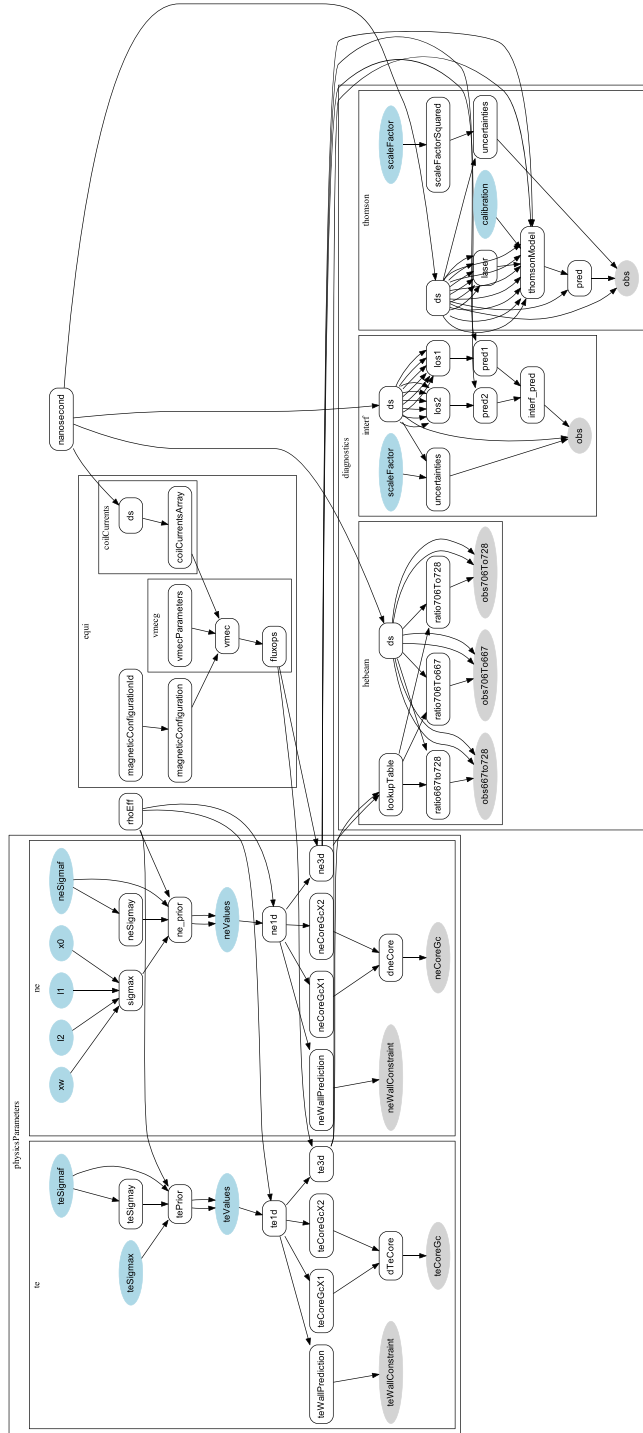


**Figure 1.** The Minerva graph for the Bayesian joint model of the DI, TS and He-BES systems at W7-X. Unknown parameters and observations are represented by blue and grey circles, respectively. Electron density,  $n_e$  and temperature,  $T_e$ , are expressed as functions of Cartesian coordinates  $x, y, z$  through coordinate transformations provided by the variational moments equilibrium code (VMEC) node. Electron density and temperature profiles are modelled using Gaussian processes along with their hyperparameters. Each model prediction is calculated based on these unknown parameters. This graph illustrates the joint probability of all unknown parameters and observations, encompassing all prior and predictive distributions.

$$\begin{aligned}
& P(n_e, T_e, \sigma_{n_e}, \sigma_{T_e}, \sigma_{DI}, \sigma_{TS}, C_{TS} | D_{DI}, D_{TS}) \\
&= \frac{P(D_{DI}, D_{TS} | n_e, T_e, \sigma_{n_e}, \sigma_{T_e}, \sigma_{DI}, \sigma_{TS}, C_{TS}) P(n_e, T_e, \sigma_{n_e}, \sigma_{T_e}, \sigma_{DI}, \sigma_{TS}, C_{TS})}{P(D_{DI}, D_{TS})} \\
&= \frac{P(D_{DI} | n_e, \sigma_{DI}) P(D_{TS} | n_e, T_e, \sigma_{TS}, C_{TS}) P(n_e | \sigma_{n_e}) P(T_e | \sigma_{T_e})}{P(D_{DI}) P(D_{TS})} \times P(\sigma_{n_e}) P(\sigma_{T_e}) P(\sigma_{DI}) P(\sigma_{TS}) P(C_{TS}), \quad (8)
\end{aligned}$$

where  $\sigma_{n_e}$  and  $\sigma_{T_e}$  are the hyperparameters of the Gaussian processes modelling the electron density and temperature profiles, respectively. The predictive distributions  $P(D_{DI} | n_e, \sigma_{DI})$  and  $P(D_{TS} | n_e, T_e, \sigma_{TS}, C_{TS})$  are modelled as Gaussian distributions, with means and standard deviations determined by the predictions of the forward models and predictive uncertainties. These uncertainties are proportional to the measurement uncertainties and are scaled by factors  $\sigma_{DI}$  and  $\sigma_{TS}$ . These scale factors, along with the calibration factor  $C_{TS}$ , are treated as additional unknown parameters due to incomplete knowledge of the measurement uncertainties. Optimising these model parameters and the hyperparameters of the Gaussian processes aims to maximise the posterior probability of the model, embodying the principle of Occam's razor [36, 37].

The calibration factor of the TS system  $C_{TS}$  is also treated as an additional unknown parameter, enabling automatic cross-calibration with the DI data. The electron density and temperature in the edge region significantly influence this cross-calibration, as the profile boundary is dependent on edge region observations. To incorporate this aspect, we use our physics and empirical knowledge to introduce *virtual* observations at the limiter/divertor positions *a priori* as part of the prior distributions, assuming the electron density and temperature are not high enough to damage the W7-X experiment's

limiter and divertor [2]. These constraints can be modelled as:

$$P(D_{wall, n_e} | n_e) = \mathcal{N}(n_e(x_{wall}, y_{wall}, z_{wall}), \sigma_{wall, n_e}^2), \quad (9)$$

$$P(D_{wall, T_e} | T_e) = \mathcal{N}(T_e(x_{wall}, y_{wall}, z_{wall}), \sigma_{wall, T_e}^2), \quad (10)$$

where  $x_{wall}$ ,  $y_{wall}$  and  $z_{wall}$  are the spatial locations of the limiter/divertor, with density and temperature constraints set to be low:  $D_{wall, n_e} = 10^{15} \text{ m}^{-3}$ ,  $\sigma_{wall, n_e} = 10^{15} \text{ m}^{-3}$ ,  $D_{wall, T_e} = 0.1 \text{ eV}$  and  $\sigma_{wall, T_e} = 0.1 \text{ eV}$ . Similarly, we introduce virtual observations to impose zero gradient constraints on the electron density and temperature profiles at the magnetic axis as follows:

$$P(D_{core, n_e} | n_e) = \mathcal{N}\left(\left.\frac{dn_e}{d\rho_{eff}}\right|_{\rho_{eff}=0}, \sigma_{core, n_e}^2\right), \quad (11)$$

$$P(D_{core, T_e} | T_e) = \mathcal{N}\left(\left.\frac{dT_e}{d\rho_{eff}}\right|_{\rho_{eff}=0}, \sigma_{core, T_e}^2\right), \quad (12)$$

where  $D_{core, n_e} = 0.0 \text{ m}^{-3}$ ,  $\sigma_{core, n_e} = 10^{18} \text{ m}^{-3}$ ,  $D_{core, T_e} = 0.0 \text{ keV}$  and  $\sigma_{core, T_e} = 0.1 \text{ keV}$ .

With these virtual observations, denoted as  $D_{v, n_e} = [D_{wall, n_e}, D_{core, n_e}]$  and  $D_{v, T_e} = [D_{wall, T_e}, D_{core, T_e}]$ , the joint posterior probability is given by:

$$\begin{aligned}
& P(n_e, T_e, \sigma_{n_e}, \sigma_{T_e}, \sigma_{DI}, \sigma_{TS}, C_{TS} | D_{DI}, D_{TS}, D_{v, n_e}, D_{v, T_e}) \\
&= \frac{P(D_{DI}, D_{TS}, D_{v, n_e}, D_{v, T_e} | n_e, T_e, \sigma_{n_e}, \sigma_{T_e}, \sigma_{DI}, \sigma_{TS}, C_{TS}) P(n_e, T_e, \sigma_{n_e}, \sigma_{T_e}, \sigma_{DI}, \sigma_{TS}, C_{TS})}{P(D_{DI}, D_{TS}, D_{v, n_e}, D_{v, T_e})} \\
&= \frac{P(D_{DI} | n_e, \sigma_{DI}) P(D_{TS} | n_e, T_e, \sigma_{TS}, C_{TS}) P(D_{v, n_e} | n_e) P(n_e | \sigma_{n_e}) P(D_{v, T_e} | T_e) P(T_e | \sigma_{T_e})}{P(D_{DI}) P(D_{TS}) P(D_{v, n_e}) P(D_{v, T_e})} \\
&\quad \times P(\sigma_{n_e}) P(\sigma_{T_e}) P(\sigma_{DI}) P(\sigma_{TS}) P(C_{TS}) \\
&= \frac{P(D_{DI} | n_e, \sigma_{DI}) P(D_{TS} | n_e, T_e, \sigma_{TS}, C_{TS}) P(n_e | D_{v, n_e}, \sigma_{n_e}) P(T_e | D_{v, T_e}, \sigma_{T_e})}{P(D_{DI}) P(D_{TS})} \times P(\sigma_{n_e}) P(\sigma_{T_e}) P(\sigma_{DI}) P(\sigma_{TS}) P(C_{TS}), \quad (13)
\end{aligned}$$

where  $P(n_e | D_{v, n_e}, \sigma_{n_e})$  and  $P(T_e | D_{v, T_e}, \sigma_{T_e})$  are the Gaussian process priors with edge and core constraints from the virtual observations. Remarkably, any physics or empirical law can be incorporated through virtual observations, treating the left-hand and right-hand sides of physics formulas

as predictions and corresponding observations, respectively. These physics/empirical priors based on virtual observations have been utilised in the Bayesian joint model at Wendelstein 7-AS [38] and for plasma equilibria at JET [6, 39].

On the other hand, local measurements of the electron density and temperature in the edge region can be provided by the He-BES system. This system injects helium gas into the plasma and collects emissions from three helium lines (667 nm, 706 nm and 728 nm). The electron density and temperature are inferred from the intensity ratios of

the 667 nm–728 nm, 706 nm–667 nm and 706 nm–728 nm helium lines, utilising pre-calculated lookup tables based on the collisional-radiative model [13, 40]. The joint posterior probability of the Bayesian joint model, including the DI, TS and He-BES systems, is expressed as:

$$\begin{aligned}
 & P(n_e, T_e, \sigma_{n_e}, \sigma_{T_e}, \sigma_{DI}, \sigma_{TS}, C_{TS} | D_{DI}, D_{TS}, D_{He}) \\
 &= \frac{P(D_{DI}, D_{TS}, D_{He} | n_e, T_e, \sigma_{n_e}, \sigma_{T_e}, \sigma_{DI}, \sigma_{TS}, C_{TS}) P(n_e, T_e, \sigma_{n_e}, \sigma_{T_e}, \sigma_{DI}, \sigma_{TS}, C_{TS})}{P(D_{DI}, D_{TS}, D_{He})} \\
 &= \frac{P(D_{DI} | n_e, \sigma_{DI}) P(D_{TS} | n_e, T_e, \sigma_{TS}, C_{TS}) P(D_{He} | n_e, T_e) P(n_e | \sigma_{n_e}) P(T_e | \sigma_{T_e})}{P(D_{DI}) P(D_{TS}) P(D_{He})} \\
 &\quad \times P(\sigma_{n_e}) P(\sigma_{T_e}) P(\sigma_{DI}) P(\sigma_{TS}) P(C_{TS}), \tag{14}
 \end{aligned}$$

where  $D_{He}$  represents the He-BES data. The predictive distribution  $P(D_{He} | n_e, T_e)$  is modelled as a Gaussian distribution, with its mean and variance derived from the lookup tables and the predictive uncertainties of the helium line ratios.

All these joint posterior distributions are explored using a Markov chain Monte Carlo (MCMC) algorithm, specifically through the use of adaptive Metropolis–Hastings algorithms [41–43], as implemented in Minerva. The hyperparameters of the Gaussian processes, alongside the model parameters, are numerically marginalised to obtain the marginal posterior distributions for the electron density and temperature profiles. This approach ensures that these profiles are inferred by considering all possible values of the hyperparameters and model parameters, thereby incorporating all measurements simultaneously in a consistent manner.

Before inferring profiles from experimental measurements, we conducted inference exercises (phantom tests) using Gaussian processes and virtual observations for both typical and hollow profile shapes, which may occur in W7-X [44]. As demonstrated in figure 2, the current setup of prior assumptions and constraints successfully infers both profile shapes.

### 3. Inference

The electron density and temperature profiles are among the most critical physics parameters for understanding the magnetohydrodynamic equilibrium, transport and performance of fusion plasma. The TS system provides these profiles across half of the plasma, with upgrades in the latest campaigns extending coverage to the full range. Meanwhile, the DI system measures the line-integrated electron density. This measurement is crucial for inferring and cross-calibrating the calibration factor of the TS system. The boundary of the profile significantly influences this cross-calibration process. Since the profile boundary is determined by the

electron density and temperature information in the edge region, this information can be sourced from virtual observations at the limiter/divertor positions or from He-BES data. In this work, profile inference was performed using various combinations of DI and TS systems, He-BES data or edge virtual observations.

Figure 3 illustrates the electron density and temperature profiles as functions of the effective minor radius  $\rho_{\text{eff}}$ , inferred by exploring the joint posterior distribution given the DI and TS data, as defined in equation (8). The dark blue lines represent the marginal posterior means, while the light blue lines depict samples from the marginal posterior distributions. These marginal posterior samples are obtained by numerically integrating the joint posterior distribution over all hyperparameters and model parameters, as expressed by:

$$\begin{aligned}
 & P(n_e, T_e | D_{DI}, D_{TS}) \\
 &= \int \int \int \int \int P(n_e, T_e, \sigma_{n_e}, \sigma_{T_e}, \sigma_{DI}, \sigma_{TS}, C_{TS} | D_{DI}, D_{TS}) \\
 &\quad \times d\sigma_{n_e} d\sigma_{T_e} d\sigma_{DI} d\sigma_{TS} dC_{TS}. \tag{15}
 \end{aligned}$$

The orange dots represent the electron density and temperature measurements with error bars from the TS analysis implemented in Minerva [8], while the green dots denote electron temperature measurements from ECE analysis on the low field side [45]. The calibration factor of the TS system  $C_{TS}$  is subject to uncertainty from experimental factors such as laser misalignment, potentially leading to discrepancies in the electron density profiles compared to the line-integrated electron density measurements from the DI. The joint model automatically adjusts the TS data with the DI measurements, aligning the electron density profiles from the joint analysis with both data sources (with the inferred calibration factor  $C_{TS} = 0.91$ ), suggesting that TS analysis might underestimate electron density by approximately 9% relative to DI data in this case. The gradient profiles for  $n_e$  and  $T_e$  are also shown in figures 3(b) and (d),

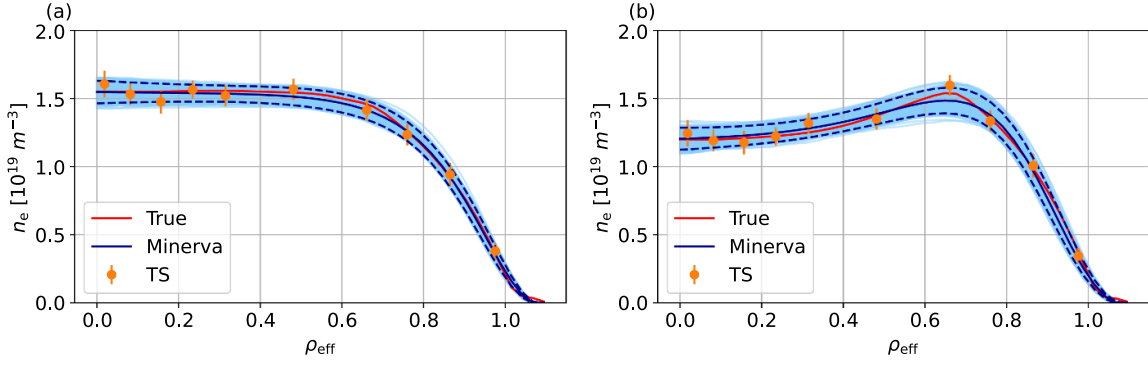


**Figure 2.** Phantom test results of the Bayesian joint model for (a) typical and (b) hollow profile shapes. The red lines represent the true underlying profiles, while the orange dots indicate synthetic TS data with error bars. The dark blue lines show the marginal posterior means calculated given the synthetic TS data, and the light blue lines illustrate samples from the marginal posterior distributions. The dashed blue lines represent the  $\pm 2\sigma$  posterior uncertainties.

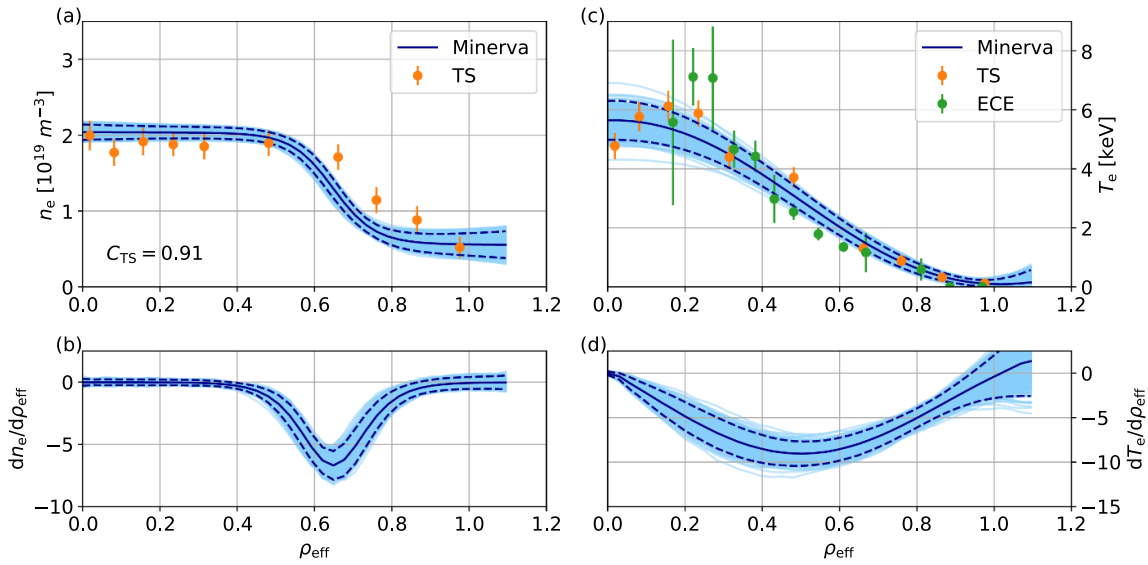


**Figure 3.** Inference results of the Bayesian joint model for the DI and TS systems (experiment ID 20160309.013,  $t = 0.43$  s): (a) electron density, (b)  $n_e$  gradient, (c) electron temperature and (d)  $T_e$  gradient profiles. The dark blue lines represent the marginal posterior means, while the light blue lines depict samples from the marginal posterior distributions. The dashed blue lines are the  $\pm 2\sigma$  posterior uncertainties. The orange dots indicate electron density and temperature measurements obtained through Bayesian analysis of TS data, with associated error bars. The green dots denote electron temperature measurements from electron cyclotron emission (ECE) analysis on the low field side. The TS system undergoes automatic cross-calibration with an inferred calibration factor  $C_{TS} = 0.91$  by the joint model. Notably, the electron density measurements from the TS system alone (orange dots) show inconsistencies with the DI data due to calibration uncertainties. The profiles produced by the joint model (dark blue lines) achieve consistency with both DI and TS data.

respectively. It is important to note that no measurements are available beyond the LCFS, i.e. for  $\rho_{\text{eff}} > 1.0$ , making the electron density and temperature in this region solely determined by the Gaussian process priors.

The electron density and temperature at the limiter/divertor positions are anticipated to be relatively low, aligning with our prior knowledge. This information can be incorporated into the model as virtual observations, as detailed in section 2. Figure 4 illustrates the electron density and temperature profiles of the marginal posterior distribution, considering these virtual observations,  $P(n_e, T_e | D_{\text{DI}}, D_{\text{TS}}, D_{V, n_e}, D_{V, T_e})$ . It is noteworthy that the calibration factors of the TS system, with and without the virtual observations, differ significantly ( $C_{TS} = 0.83$  with

virtual observations versus  $C_{TS} = 0.91$  without), indicating a substantial impact of edge region data on the calibration factor.

To compare inference outcomes of the joint model based on virtual observations with those obtained from experimental observations in the edge region, He-BES data is incorporated into the joint model instead of virtual observations. The electron density and temperature profiles from the marginal posterior distribution, given the He-BES data  $P(n_e, T_e | D_{\text{DI}}, D_{\text{TS}}, D_{\text{He}})$ , are depicted in figure 5. The calibration factor derived with He-BES data ( $C_{TS} = 0.86$ ) exhibits a slight deviation from that obtained using virtual observations ( $C_{TS} = 0.83$ ). Figure 6 compares the predictions based



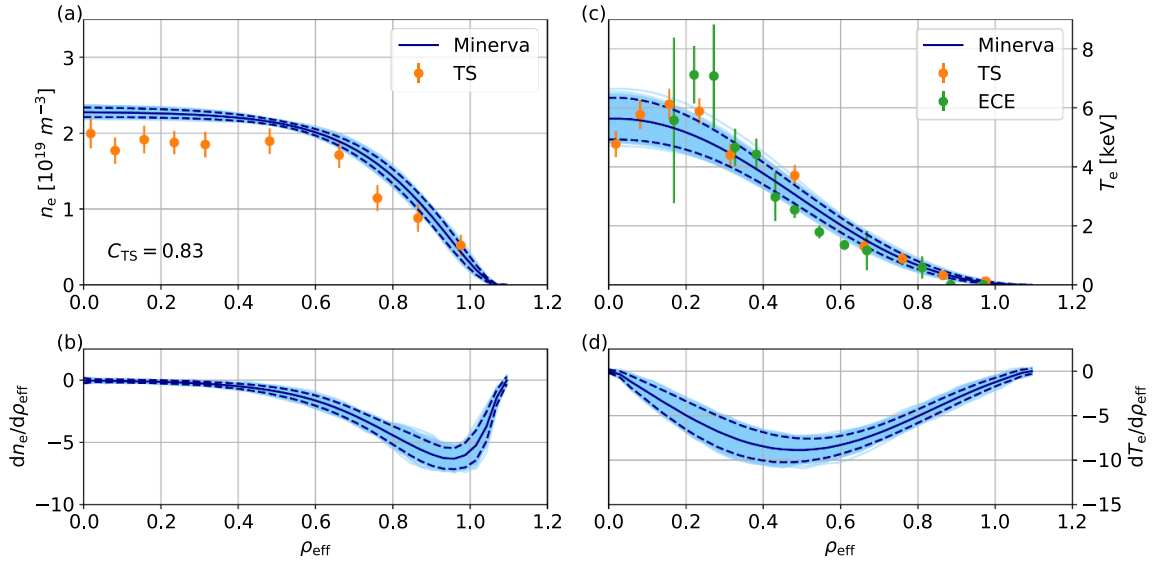


**Figure 4.** Similar to figure 3, presenting inference results of the Bayesian joint model of the DI and TS systems, now including electron density and temperature constraints at the limiter/divertor positions through virtual observations.

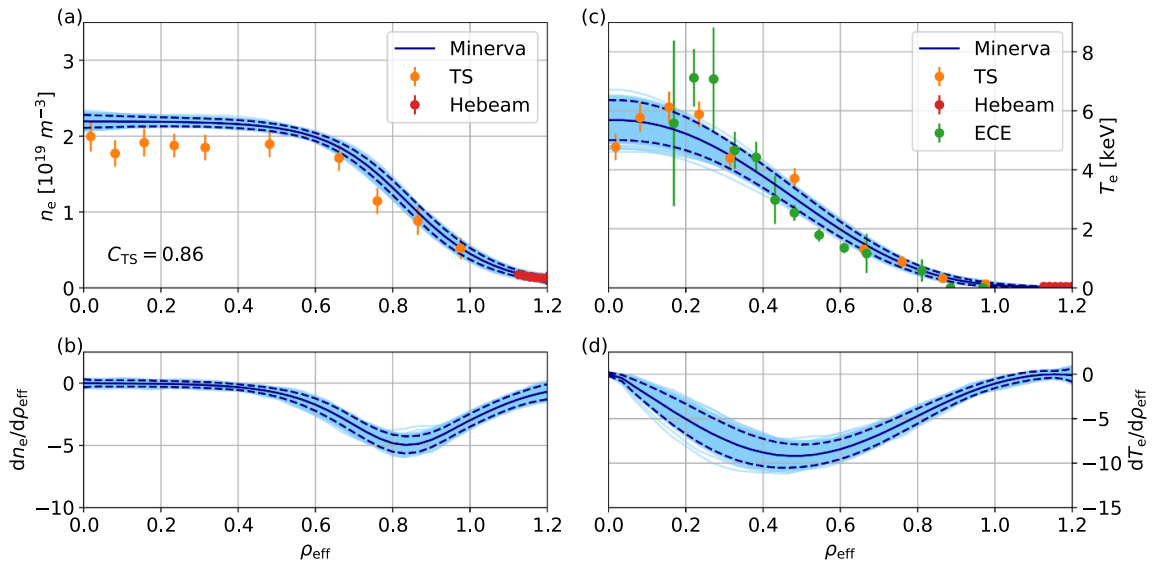


**Figure 5.** Similar to figure 3, showing inference results of the Bayesian joint model of the DI, TS and He-BES systems. The red dots represent electron density and temperature measurements from a standalone Bayesian analysis of the helium beam model developed in this work.

on these marginal posterior means and samples against the corresponding observations. The absolute differences between the DI data and predictions with He-BES data and virtual observations are  $0.101 \times 10^{12} \text{ m}^{-2}$  and  $0.184 \times 10^{12} \text{ m}^{-2}$ , respectively, while the DI measured data is  $2.30 \times 10^{19} \text{ m}^{-2} \pm 5.33 \times 10^{14} \text{ m}^{-2}$ . Both predictions match well with the DI data within the uncertainties, which implies that the cross-calibration was performed properly in both cases. The He-BES system not only yields density and temperature measurements but also provides their measurement uncertainties in the edge region, which are crucial for determining the optimal hyper-parameters (smoothness) through Bayesian Occam's razor [36, 37].

Both the edge profiles obtained from virtual observations and He-BES data are valid solutions, given different combinations of assumptions, constraints and observations. The joint model integrating the DI, TS and He-BES systems generates plausible electron density and temperature profiles in the edge region, with He-BES providing direct measurements. In contrast, virtual observations rely on synthetic constraints to infer edge profiles, which, while valuable, are derived indirectly by excluding empirically unreasonable solutions (high density and temperature at the limiter/divertor). When direct observations are scarce, virtual observations offer an alternative means to bolster the model and rule out solutions that are physically or empirically implausible.

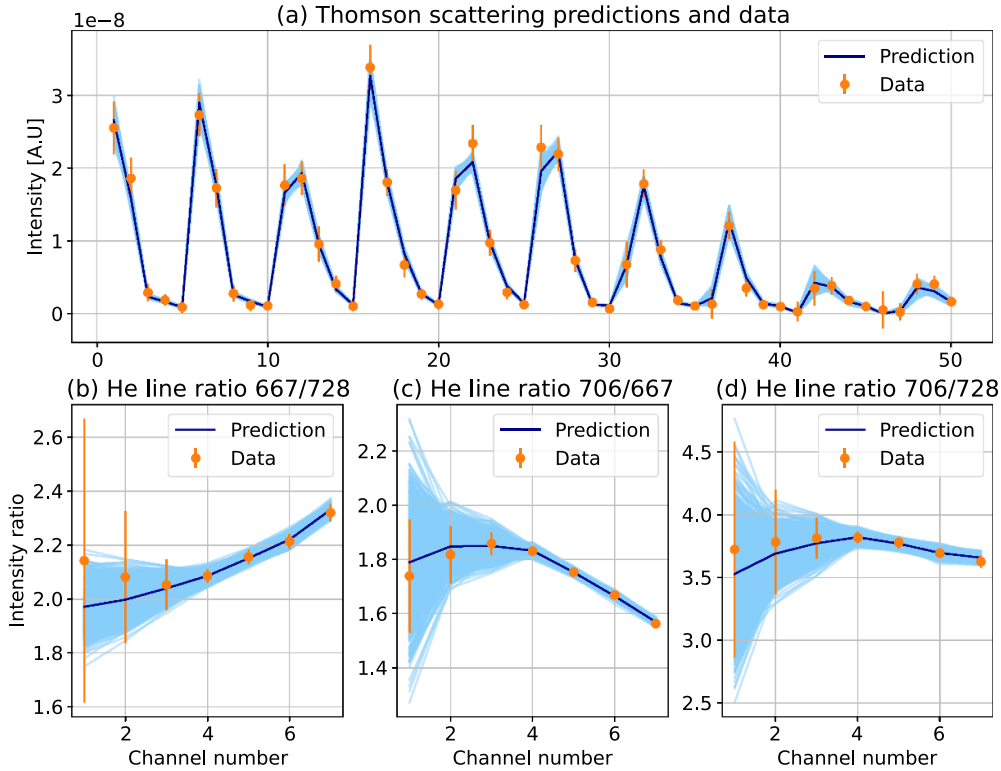


**Figure 6.** Comparisons of predictions (in dark blue and light blue) against observations (in orange) from (a) TS data and (b) 667 nm–728 nm, (c) 706 nm–667 nm and (d) 706 nm–728 nm helium line intensity ratios, based on the posterior mean and samples shown in figure 5. The TS data comprise 50 data points across ten spatial locations, with five integrated signals over different spectral ranges for each location. The He-BES data consists of the ratios of line intensities from eight spatial locations.

**Table 1.** Gaussian process hyperparameters (maximum *a posteriori*).

Data	$\sigma_{f,n_e}$	$\sigma_{x,n_e}^{\text{core}}$	$\sigma_{x,n_e}^{\text{edge}}$	$\rho_{\text{eff},0,n_e}$	$\rho_{\text{eff},w,n_e}$	$\sigma_{f,T_e}$	$\sigma_{x,T_e}$
$D_{\text{DI}}, D_{\text{TS}}, D_{v,n_e}, D_{v,T_e}$	2.11	31.0	15.0	0.735	0.133	3.29	0.539
$D_{\text{DI}}, D_{\text{TS}}, D_{\text{He}}$	2.43	25.8	10.8	0.782	0.223	2.89	0.523

The hyperparameters of the Gaussian processes are shown in table 1. As expected, the core length scale  $\sigma_{x,n_e}^{\text{core}}$  is larger than the edge length scale  $\sigma_{x,n_e}^{\text{edge}}$ , indicating that the core profiles are flatter while the edge profiles are steeper. The length scale transition positions  $\rho_{\text{eff},0,n_e}$  inferred from the He-BES data and the virtual observations are similar. In addition, due to the globally optimised length scale (profile smoothness) and the zero gradient constraints at the magnetic axis, the inferred profiles do not capture minor structures. For instance, the data sets presented in this work may suggest a peak in  $T_e$  at  $\rho=0.2$ . Nonetheless, given the limited number of measurement points and the magnitude of observational uncertainties, the optimised smoothness and core constraints prevent the model from fitting this minor structure, thereby avoiding potential overfitting.

We emphasise that the inferred profiles neither underfit nor overfit the data. Bayesian methods automatically and quantitatively penalise underfitted and overfitted models. Underfitted models, which suggest overly simplistic profiles such as straight lines, fail to predict the data within their predictive

uncertainties. On the contrary, overfitted models, which suggest overly complex profiles, for example, ones with excessive fluctuations, might predict the data more accurately than simpler models. However, overfitted models can generate a wide variety of profiles, with each being almost equally probable. Consequently, the probability associated with any single proposed profile is lower than that of profiles proposed by simpler models, given that the total probability across the entire profile space must sum to one. Thus, overly complex models are automatically self-penalised by Bayesian Occam's razor [36, 37]. Specifically, Gaussian processes with excessively small length scales (overly complex models) can suggest profiles that accurately predict the data, i.e. with high predictive probabilities  $P(D_{\text{DI}}|n_e, \sigma_{\text{DI}})$ ,  $P(D_{\text{TS}}|n_e, T_e, \sigma_{\text{TS}}, C_{\text{TS}})$  and  $P(D_{\text{He}}|n_e, T_e)$ , but the prior probabilities of these profiles  $P(n_e|\sigma_{n_e})$  and  $P(T_e|\sigma_{T_e})$  are low because the Gaussian processes can propose many other equally probable profiles. Therefore, the joint posterior probability for overly complex models is diminished. Models characterised by excessively large predictive uncertainties are similarly penalised. By

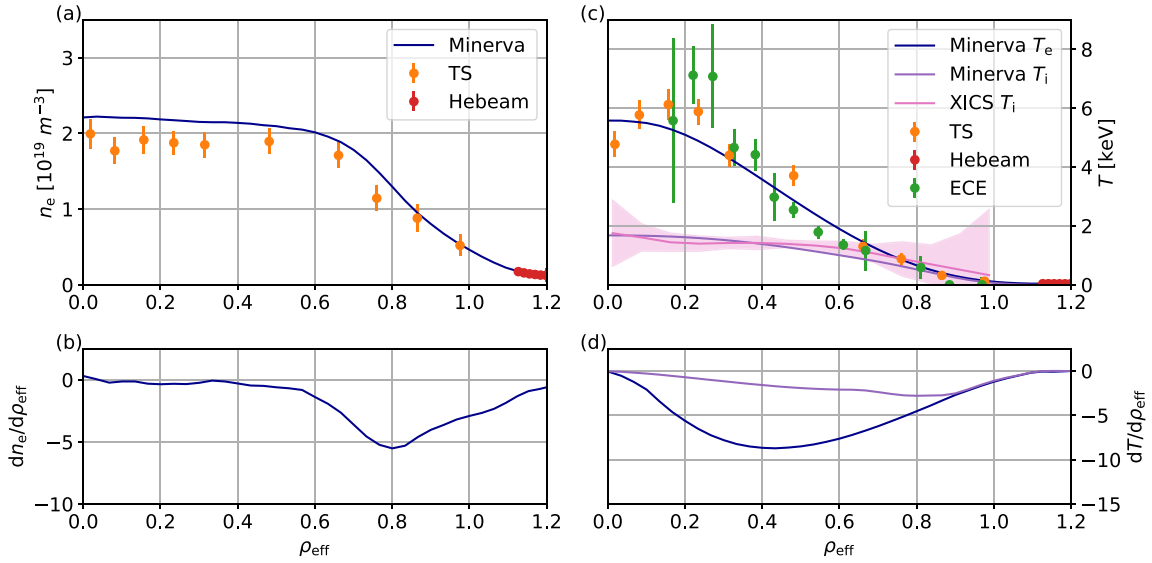


**Figure 7.** Similar to figure 3, this figure presents inference results from the Bayesian joint model integrating data from the DI, TS, He-BES and XICS systems. The ion temperature and its gradient profiles are represented by the purple lines in (c) and (d). The ion temperature profiles with the  $\pm 2\sigma$  posterior uncertainties from the Minerva XICS inference, are shown in pink.

exploring the joint posterior distribution of the electron density and temperature profiles, along with hyperparameters and model parameters, we identify profiles with appropriate length scales (smoothness) and predictive uncertainties. Moreover, the inference outcomes yield marginal posterior samples and uncertainties that consider all possible values of hyperparameters and model parameters, meaning these samples and uncertainties are robust to specific hyperparameter and model parameter values.

#### 4. The addition of the XICSs

The XICSs [14, 15] are utilised to measure x-ray spectra of argon and iron impurities in various charge states, encompassing a wide electron temperature range from 0.3 keV to 6 keV. The XICS system captures line-integrated spectra along 20 lines of sight, covering over half of the plasma's poloidal cross-section at a toroidal angle of 159.09 degrees. The forward model for XICS, previously implemented in Minerva [14], has been incorporated into the Bayesian joint model alongside the DI, TS and He-BES systems. This forward model computes local x-ray spectra considering various atomic processes, including excitation, recombination, ionization and charge exchange, which are influenced by the electron density and temperature as well as the ion temperature. These predicted local spectra are then integrated along the lines of sight by the forward model to produce the line-integrated x-ray spectra, based on the aforementioned physics parameters.

The ion temperature prior distribution is modelled as a Gaussian process with zero mean and a squared exponential covariance function. The joint posterior probability, incorporating data from the DI, TS, He-BES and XICS, can be expressed as:

$$\begin{aligned}
 &P(n_e, T_e, T_i, \sigma_{n_e}, \sigma_{T_e}, \sigma_{T_i}, \sigma_{DI}, \sigma_{TS}, C_{TS} | D_{DI}, D_{TS}, D_{He}, D_{XICS}) \\
 &= \frac{P(D_{XICS} | n_e, T_e, T_i) P(T_i | \sigma_{T_i}) P(\sigma_{T_i})}{P(D_{XICS})} \\
 &\quad \times P(n_e, T_e, \sigma_{n_e}, \sigma_{T_e}, \sigma_{DI}, \sigma_{TS}, C_{TS} | D_{DI}, D_{TS}, D_{He}), \quad (16)
 \end{aligned}$$

where  $T_i$  represents the ion temperature,  $\sigma_{T_i}$  denotes the hyperparameters of the Gaussian process, and  $D_{XICS}$  refers to the XICS data. The predictive distribution  $P(D_{XICS} | n_e, T_e, T_i)$  is modelled as a Gaussian distribution, with mean and variance derived from the XICS forward model, reflecting the predictive uncertainties of the line-integrated x-ray spectra. The electron density, electron temperature and ion temperature profiles are inferred tomographically based on the combined data from the DI, TS, He-BES and XICS systems.

The maximum *a posteriori* (MAP) solutions for the electron density and temperature, along with ion temperature profiles, are determined using the pattern search algorithm [46] implemented in Minerva, as illustrated in figure 7. The ion temperature profiles with the  $\pm 2\sigma$  posterior uncertainties from the Minerva XICS inference [15], are shown in pink. Comparisons between the model predictions and observations from the helium beam emission and line-integrated x-ray spectra are depicted in figure 8. Due to the substantial complexity and computational demands of the XICS forward model, comprehensive sampling from the joint posterior distribution is deferred to future investigations. This challenge may be addressed by employing a neural network to approximate the XICS model within Minerva [20, 22].

Remarkably, we infer these profiles with optimal values of hyperparameters (indicating smoothness) and model parameters by maximising the joint posterior probability. Traditionally, optimising hyperparameters and model parameters involves maximising their posterior probability, which

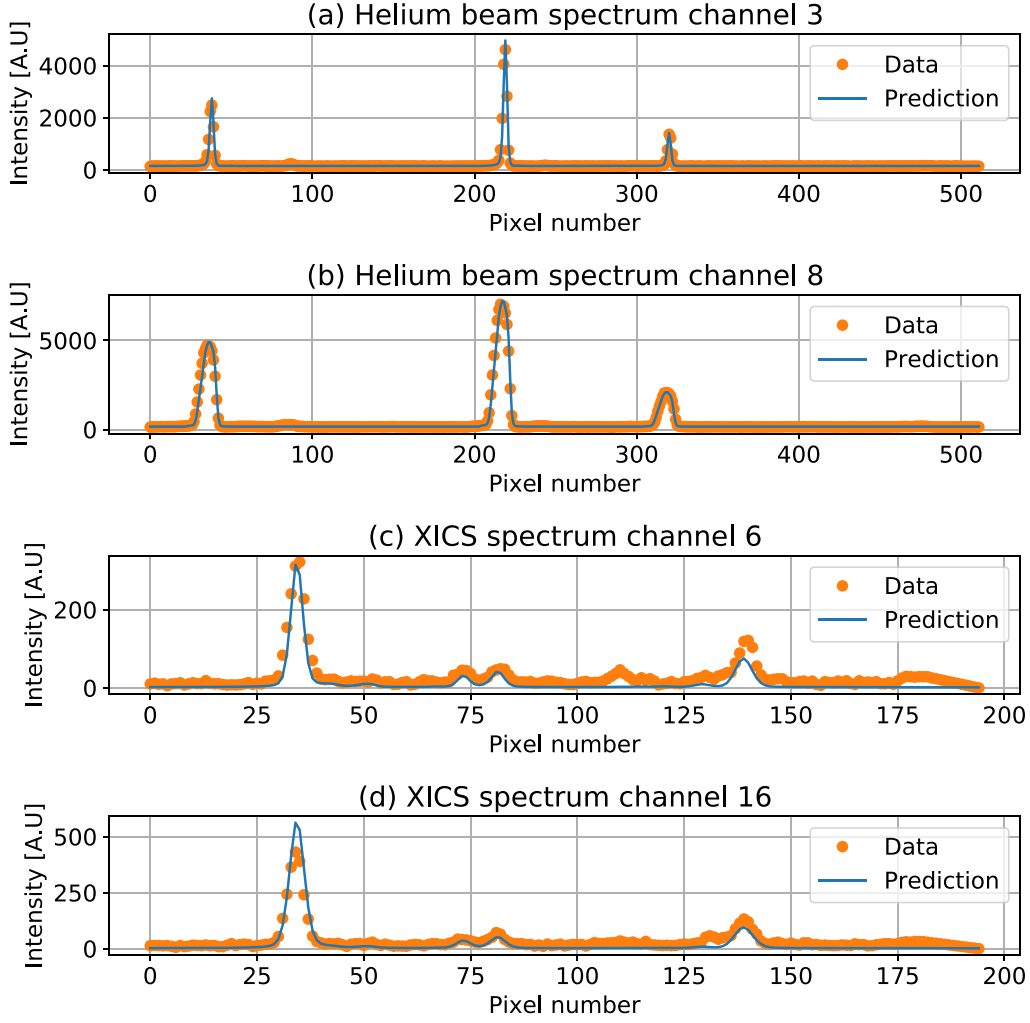


**Figure 8.** Predictions (in blue) versus observations (in orange) for helium beam spectra from channel #3 (near the divertor) and #8 (the innermost channel), along with XICS spectra from channel #6 (in the edge region) and #16 (in the core region), based on the profiles depicted in figure 7.

is proportional to the marginal predictive distribution of the observations, also referred to as the model evidence. Calculating the model evidence poses a significant computational challenge due to the necessity of integrating over a high-dimensional parameter space, representing a substantial hurdle for applying Bayesian Occam's razor in real-world applications. On the other hand, the computation of the joint posterior probability does not require such integration. The joint posterior distribution is conceptualised as the product of the conditional posterior distribution of the parameters given the hyperparameters and model parameters, and the posterior distribution of these hyperparameters and model parameters themselves, expressed as:

$$\begin{aligned}
 &P(n_e, T_e, T_i, \sigma_{n_e}, \sigma_{T_e}, \sigma_{T_i}, \sigma_{D_I}, \sigma_{T_S}, C_{T_S} | D_{D_I}, D_{T_S}, D_{He}, D_{XICS}) \\
 &= P(n_e, T_e, T_i | \sigma_{n_e}, \sigma_{T_e}, \sigma_{T_i}, \sigma_{D_I}, C_{T_S}, \sigma_{T_S}, D_{D_I}, D_{T_S}, D_{He}, D_{XICS}) \\
 &\quad \times P(\sigma_{n_e}, \sigma_{T_e}, \sigma_{T_i}, \sigma_{D_I}, \sigma_{T_S}, C_{T_S} | D_{D_I}, D_{T_S}, D_{He}, D_{XICS}). \quad (17)
 \end{aligned}$$

The joint posterior distribution inherently applies Bayesian Occam's razor via the posterior probabilities of the hyperparameters and model parameters. Consequently, the MAP solutions yield profiles that are optimally smooth rather than overly complex or wiggly, as evidenced in figure 7.

## 5. Conclusions

The Bayesian joint model, integrating data from the interferometer, TS and He-BES systems, has been developed for W7-X. Each forward model was individually implemented and then unified within the Minerva framework. The electron density and temperature profiles, modelled as functions of the effective minor radius using Gaussian processes, include hyperparameters and model parameters such as the calibration factor of the TS system as additional unknowns. The exploration of the joint posterior distribution of these profiles,

hyperparameters and model parameters leverages a MCMC algorithm.

Profile inference utilised varying combinations of the three distinct data sets alongside virtual observations. Specifically, electron density and temperature profiles were inferred using the joint model of the interferometer and TS system, with automatic cross-calibration against line-integrated electron density measurements from the interferometer. Virtual observations were introduced as part of the prior distributions to exclude physically and empirically unlikely solutions, particularly assumptions regarding non-excessive electron density and temperature at limiter/divertor positions. The profiles and calibration factor inferred from the joint posterior distribution with virtual observations were found to be physically and empirically consistent, differing significantly from those inferred without such observations due to the absence of edge region data.

Furthermore, to contrast inference solutions based on virtual versus experimental observations in the edge region, helium beam emission data was incorporated into the model in place of virtual observations. The profiles inferred from the comprehensive model—comprising data from the interferometer, TS and helium beam emission systems—were deemed reasonable. This is attributed to the helium beam data providing not only electron density and temperature measurements but also their uncertainties in the edge region, critical for determining optimal profile smoothness via Bayesian Occam's razor. Nevertheless, virtual observations remain a viable alternative to strengthen the model and eliminate unlikely inference solutions when empirical data is limited.

These inference solutions, characterised by optimal hyperparameters (smoothness) and model parameters as dictated by Bayesian Occam's razor, avoid the pitfalls of over-complex models. This approach ensures that the inference solutions neither underfit nor overfit the measurements. The marginal posterior samples, reflecting electron density and temperature profiles, incorporate all conceivable values of the hyperparameters and model parameters relative to the observations. The joint posterior distribution, central to Bayesian Occam's razor, simplifies the calculation of joint posterior probabilities compared to model evidence, facilitating the application of Bayesian principles in real-world scenarios. As demonstrated, the MAP solutions from the joint posterior probability distribution, considering data from the interferometer, TS, He-BES and XICS systems, yield electron density, temperature and ion temperature profiles with suitable model parameters and hyperparameters, thereby achieving a balance between fitting the data and maintaining model simplicity.

## Acknowledgments

This work has been carried out within the framework of the EUROfusion Consortium, funded by the European Union via the Euratom Research and Training Programme (Grant Agreement No. 101052200—EUROfusion). Views and opinions expressed are however those of the author(s) only and do not necessarily reflect those of the European Union or the

European Commission. Neither the European Union nor the European Commission can be held responsible for them.

This work is supported by National R&D Program through the National Research Foundation of Korea (NRF) funded by the Ministry of Science and ICT (Grant Nos. RS-2022-00155917 and NRF-2021R1A2C2005654).

## ORCID iDs

Sehyun Kwak  <https://orcid.org/0000-0001-7874-7575>

U. Hoefel  <https://orcid.org/0000-0003-0971-5937>

A. Langenberg  <https://orcid.org/0000-0002-2107-5488>

Y.-C. Ghim  <https://orcid.org/0000-0003-4123-9416>

## References

- [1] Litaudon X. *et al* 2017 *Nucl. Fusion* **57** 102001
- [2] Klinger T. *et al* 2019 *Nucl. Fusion* **59** 112004
- [3] Seed eScience Research 2024 The Minerva framework (available at: <https://seed-escience.org/>)
- [4] Pearl J. 1988 *Probabilistic Reasoning in Intelligent Systems: Networks of Plausible Inference* (Morgan Kaufmann)
- [5] Svensson J. and Werner A. 2008 *Plasma Phys. Control. Fusion* **50** 085002
- [6] Ford O.P. 2010 Tokamak plasma analysis through Bayesian diagnostic modelling *PhD Thesis* Imperial College London
- [7] Svensson J. (JET-EFDA, Culham Science Centre) 2011 *JET Report EFDA-JET-PR(11)24* (available at: <https://scipub.euro-fusion.org/wp-content/uploads/eurofusion/EFDP11024.pdf>)
- [8] Bozhnikov S. *et al* 2017 *J. Instrum.* **12** 10004
- [9] Kwak S., Svensson J., Bozhnikov S.A., Flanagan J., Kempenaars M., Boboc A. and Ghim Y.-C. 2020 *Nucl. Fusion* **60** 046009
- [10] Li D., Svensson J., Thomsen H., Medina F., Werner A. and Wolf R. 2013 *Rev. Sci. Instrum.* **84** 083506
- [11] Schilling J., Thomsen H., Brandt C., Kwak S. and Svensson J. 2021 *Plasma Phys. Control. Fusion* **63** 055010
- [12] Kwak S., Svensson J., Brix M. and Ghim Y.-C. 2016 *Rev. Sci. Instrum.* **87** 023501
- [13] Kwak S., Svensson J., Brix M. and Ghim Y.-C. 2017 *Nucl. Fusion* **57** 036017
- [14] Langenberg A., Svensson J., Thomsen H., Marchuk O., Pablant N.A., Burhenn R. and Wolf R.C. 2016 *Fusion Sci. Technol.* **69** 560–7
- [15] Langenberg A. *et al* 2019 *Rev. Sci. Instrum.* **90** 063505
- [16] Hoefel U. *et al* 2019 *Rev. Sci. Instrum.* **90** 043502
- [17] Pavone A. *et al* 2019 *J. Instrum.* **14** C10003
- [18] Kwak S. *et al* 2021 *Rev. Sci. Instrum.* **92** 043505
- [19] Mora H.T. *et al* 2017 FPGA acceleration of Bayesian model based analysis for time-independent problems 2017 *IEEE Global Conf. on Signal and Information Processing (GlobalSIP)* (IEEE) pp 774–8
- [20] Pavone A., Svensson J., Langenberg A., Pablant N., Hoefel U., Kwak S. and Wolf R.C. 2018 *Rev. Sci. Instrum.* **89** 10K102
- [21] Pavone A., Svensson J., Langenberg A., Höfel U., Kwak S., Pablant N. and Wolf R.C. 2019 *Plasma Phys. Control. Fusion* **61** 075012
- [22] Pavone A., Merlo A., Kwak S. and Svensson J. 2023 *Plasma Phys. Control. Fusion* **65** 053001
- [23] Knauer J., Kornejew P., Trimino Mora H., Hirsch M., Werner A. and Wolf R.C. (The W7-X Team) 2016 A new dispersion interferometer for the stellarator Wendelstein 7-X *Proc. 43rd EPS Conf. on Plasma Physics* ed P. Mantica (European Physical Society)

- [24] Barbui T., Krychowiak M., König R., Schmitz O., Muñoz B., Schweer B. and Terra A. 2016 *Rev. Sci. Instrum.* **87** 11E554
- [25] Jaynes E.T. 2003 *Probability Theory: The Logic of Science* (Cambridge University Press)
- [26] Devinderjit Sivia J.S. 2006 *Data Analysis: A Bayesian Tutorial* (Oxford University Press)
- [27] O'Hagan A. 1978 *J. R. Stat. Soc. B* **40** 1–42
- [28] Neal R.M. 1995 Bayesian learning for neural networks *PhD Thesis* University of Toronto
- [29] Rasmussen C.E. and Williams C.K.I. 2006 *Gaussian Processes for Machine Learning* (MIT Press)
- [30] Chilenski M., Greenwald M., Marzouk Y., Howard N., White A., Rice J. and Walk J. 2015 *Nucl. Fusion* **55** 023012
- [31] Chen J. *et al* 2023 *Plasma Phys. Control. Fusion* **65** 055027
- [32] Higdon D., Swall J. and Kern J. 1999 Non-stationary spatial modeling *Bayesian Statistics 6 Proc. 6th Valencia Int. Meeting* pp 761–8
- [33] Hirshman S., van RIJ W. and Merkel P. 1986 *Comput. Phys. Commun.* **43** 143–55
- [34] Geiger J., Beidler C., Drevlak M., Maaßberg H., Nührenberg C., Suzuki Y. and Turkin Y. 2010 *Contrib. Plasma Phys.* **50** 770–4
- [35] Naito O., Yoshida H. and Matoba T. 1993 *Phys. Fluids B* **5** 4256–8
- [36] Gull S.F. 1988 Bayesian inductive inference and maximum entropy *Maximum-Entropy and Bayesian Methods in Science and Engineering: Foundations* ed G.J. Erickson and C.R. Smith (Springer) pp 53–74
- [37] Mackay D.J. 1991 Bayesian methods for adaptive models *PhD Thesis* California Institute of Technology
- [38] Svensson J., Dinklage A., Geiger J., Werner A. and Fischer R. 2004 *Rev. Sci. Instrum.* **75** 4219–21
- [39] Kwak S., Svensson J., Ford O.P., Appel L. and Ghim Y.-C. (JET Contributors) 2022 *Nucl. Fusion* **62** 126069
- [40] Krychowiak M., Brix M., Dodt D., Feng Y., König R., Schmitz O., Svensson J. and Wolf R. 2011 *Plasma Phys. Control. Fusion* **53** 035019
- [41] Metropolis N., Rosenbluth A.W., Rosenbluth M.N., Teller A.H. and Teller E. 1953 *J. Chem. Phys.* **21** 1087–92
- [42] Hastings W.K. 1970 *Biometrika* **57** 97–109
- [43] Haario H., Saksman E. and Tamminen J. 2001 *Bernoulli* **7** 223
- [44] Beidler C.D., Feng Y., Geiger J., Köchl F., Maaßberg H., Marushchenko N.B., Nührenberg C., Smith H.M. and Turkin Y. 2018 *Plasma Phys. Control. Fusion* **60** 105008
- [45] Hirsch M. *et al* 2019 *EPJ Web Conf.* **203** 03007
- [46] Hooke R. and Jeeves T.A. 1961 *J. ACM* **8** 212–29